Optics Letters

Three-dimensional dynamic measurement of irregular stringy objects via digital holography

Longchao Yao,[1,2] Jun Chen,[1,*] Paul E. Sojka,[1] Xuecheng Wu,[2] and Kefa Cen[2]

[1]School of Mechanical Engineering, Purdue University, West Lafayette, Indiana 47906, USA
[2]State Key Laboratory of Clean Energy Utilization, Zhejiang University, Hangzhou 310027, China
*Corresponding author: junchen@purdue.edu

Received 12 January 2018; accepted 6 February 2018; posted 15 February 2018 (Doc. ID 319633); published 8 March 2018

Dynamic stringy objects such as liquid rims and ligaments are frequently observed in important applications such as the multiphase breakup of fuel droplets. We develop a new method based on digital in-line holography to automatically measure complicated stringy objects. A static spring mounted on a rotator is measured to validate the effectiveness and accuracy of the method. The sections are extracted along the skeleton of the spring in a depth-of-field extended image and then sized and located as individual particles using a hybrid method. The surface points of sections are stitched together to visualize the entire spring. Local thickness errors smaller than 5.3%, and z errors smaller than 230 μm are achieved. This method is applied to characterize the spatial-temporal features of the liquid rim formed in the bag-type regime of the aerodynamic breakup of a falling drop. The evolution of the rim/ligament structures is continuously captured in seven frames, lasting in 1.58 ms. This Letter extends the application of digital holography as an effective 3D diagnostic tool.

OCIS codes: (090.1995) Digital holography; (120.0120) Instrumentation, measurement, and metrology; (100.6890) Three-dimensional image processing.

https://doi.org/10.1364/OL.43.001283

Digital in-line holography (DIH) is an effective tool for measuring three-dimensional (3D) objects in various fields such as multiphase flow, combustion, physical oceanography, and microorganisms (e.g., [1]). It has been applied to quantify solid particles [2,3], liquid droplets [4,5], and bubbles [6]. The hologram digitally records the interference pattern formed by the object wave (scattered from objects) and the reference wave (the undisturbed part of the incident wave). Then it is processed numerically by simulating light propagation to reconstruct the 3D objects at different depth distances. To quantify the dimension and location of objects (e.g., particles or bubbles), a variety of auto-detection and auto-focusing algorithms were developed by examining, from the reconstructed wave fields, the intensity [6], sharpness [7], correlation coefficient [4], etc.

These methods, however, are not suitable for the stringy objects which usually have a high aspect ratio and span a long distance in the field of view. Stringy objects are frequently observed in a variety of applications and need to be accurately characterized experimentally in a non-invasive way. For instance, when liquid fuel is atomized in the combustor, string-shaped rims and ligaments are first formed before fragmenting into fine droplets (e.g., [8]). In pulverized coal combustion, a devolatilization product ejected from the parent particle accumulates into stringy objects, which are crucial for soot accumulation [3]. Understanding the dynamic evolution of these structures and the relevant underlying physics are of keen interest in these fields. Previous applications of DIH in these fields focused only on characterizing the droplets formed by secondary breakup processes or the coal particles, both of which can be effectively approximated as spherical objects. Quantifying the stringy objects, relying heavily on manual operations, is labor extensive and lacks accuracy. To the best of our knowledge, DIH for automated measurement of stringy objects is constrained to simple cases such as fibers and needle shaped entities. Lebrun *et al.* [9] refocused a fiber in a single reconstructed image by reconstructing the hologram in a tilted plane, with two key assumptions: (a) the fiber is straight, and (b) the tilted angle of the fiber is known. A point cloud method was later developed by Khanam *et al.* [10] to measure the tilt of the fiber and needle without such knowledge of the object. In each reconstructed plane at a different depth location, a low gray-scale threshold was used to retrieve the focused part of the object. However, in this method, the gray-scale threshold must be set to a very low value; thus the darkest portion of the reconstructed field is identified, and the diameter of the object cannot be retrieved. In addition, it is only applicable to straight objects such as fibers or needles.

In this Letter, we report a method to automatically characterize an irregular 3D stringy object using DIH. The holograms of an arbitrarily developed stringy object are recorded by a high-speed DIH system. A depth-of-field extended image (DEI) is first obtained by applying an image fusion algorithm to reconstructed images at different depths [2]. The edge and the skeleton of the object are extracted in two-dimensional (2D) space. The object is divided into small sections along the skeleton, and a hybrid method [11] is applied to measure

the size and 3D location of each section. All the sections are then stitched together to retrieve the entire object. The method is first validated by measuring a stationary object and then applied to a dynamic structure.

The setup for the static calibration is shown in Fig. 1. A diode-pumped solid-state laser (Laser Lab Components, Inc., SLM532-300; wavelength of 532 nm, 300 mW) is spatially filtered and expanded into a 5 cm diameter plane wave. It travels through the sample volume where a stringy object (spring) is mounted on a rotation stage. The hologram is recorded by a charge-coupled device camera (IMPERX ICL-B4020, $4,008 \times 2,672$ pixels, $9 \times 9\ \mu m^2$/pixel). The object is $d = 164$ mm away from the camera. Unlike the straight fiber and needle studied previously [9,10], the helical spring winds its way three-dimensionally, with detailed parameters shown in Fig. 1(b).

Figure 2(a) shows a typical hologram of the spring, which can be reconstructed by the angular spectral method

$$E_r(k,l,z_r) = \mathcal{F}^{-1}\left\{\mathcal{F}[R \cdot h(m,n)] \times \exp\left[-j\frac{2\pi z_r}{\lambda}\sqrt{1-\left(\frac{\lambda m}{M\Delta x}\right)^2-\left(\frac{\lambda n}{N\Delta y}\right)^2}\right]\right\}, \quad (1)$$

where $\mathcal{F}$ and $\mathcal{F}^{-1}$ represent Fourier transform and inverse Fourier transform, respectively; E_r is the reconstructed complex amplitude at distance z_r; and R is the reference wave ($R = 1$ for in-line holography). $h(m,n)$ is the digitalized hologram ($M \times N$ pixels, pixel size of $\Delta x \times \Delta y$), and (k,l) and (m,n) label the pixels on the reconstructed image and the original hologram, respectively. A sequence of reconstructions is performed at a depth range (160 mm $< z_r <$ 170 mm) with a 50 μm step, and the reconstructed field is analyzed to measure the spring. To extract a 2D projection of the spring, a wavelet-based image fusion algorithm [2] is adopted to generate a DEI. Then a gray-scale threshold, 0.3 based on a normalized gray scale [from 0 (black) to 1 (white)], is applied to binarize the DEI for extracting the edge and 2D skeleton of the object which are shown in Fig. 2(b). The object is then segmented into a total of S sections (detailed below), and the hybrid method [11] is applied to determine the corresponding z-location of each section. In the hybrid method, a series of thresholds is applied to each section in the DEI, and an optimal one is identified by maximizing sharpness on the candidate edges. Then the corresponding edge is identified from different reconstruction planes along the z direction.

The object in the DEI is segmented into a total of S sections [one pitch in the dashed box of Fig. 2(a) is exemplified in Figs. 2(b) and 2(c)], where the ith section has a geodesic distance $\zeta_i = (i-1)\Delta\zeta_i$, $(i = 1, 2, \ldots, S)$ from one of the endpoints of the skeleton. $\Delta\zeta_i = 30$ pixels are adopted for the spring measurement, and 103 sections are processed in the solid box region in Fig. 2(a). The 2D orientation of the ith section in DEI is described by the vector

$$(\delta x_i, \delta y_i) = \delta\mathbf{x}_i = \begin{cases} \mathbf{x}_2 - \mathbf{x}_1 & i = 1 \\ \dfrac{(\mathbf{x}_{i+1} - \mathbf{x}_{i-1})}{2} & \text{if } 1 < i < S, \\ \mathbf{x}_S - \mathbf{x}_{S-1} & i = S \end{cases} \quad (2)$$

where $\mathbf{x}_i = (x_i, y_i)$ is the coordinate of the ith section. As shown in Figs. 2(b) and 2(d), the normal direction (white line perpendicular to the skeleton), (X_i, Y_i), perpendicular to $(\delta x_i, \delta y_i)$ at section center (x_i, y_i), satisfies $(X_i - x_i)\delta x_i + (Y_i - y_i)\delta y_i = 0$. In practice, $(X_i - x_i)\delta x_i + (Y_i - y_i)\delta y_i < O$ is adopted because the coordinates of a digital image are discretized ($O = 100$ pixels used in this Letter). Along the normal direction, there are two points, $(x_i^{p_1}, y_i^{p_1})$ and $(x_i^{p_2}, y_i^{p_2})$, intersecting with the edges in the DEI, indicated by red dots in Figs. 2(b) and 2(d). This section is described by a distance $\eta_i = \sqrt{(x_i^{p_1} - x_i^{p_2})^2 + (y_i^{p_1} - y_i^{p_2})^2}$ (unit: pixels) and an angle $\theta_i = \arctan[(y_i^{p_2} - y_i^{p_1})/(x_i^{p_2} - x_i^{p_1})]$. A rectangle mask (width $w_i = \eta_i + 20$, height $2\Delta\zeta_i$, unit: pixels) with four corners A, B, C, and D,

$$\begin{bmatrix} x_i^A & y_i^A \\ x_i^B & y_i^B \\ x_i^C & y_i^C \\ x_i^D & y_i^D \end{bmatrix}' = \begin{bmatrix} \cos\theta_i & -\sin\theta_i \\ \sin\theta_i & \cos\theta_i \end{bmatrix} \begin{bmatrix} -w_i/2 & -\Delta\zeta_i \\ w_i/2 & -\Delta\zeta_i \\ w_i/2 & \Delta\zeta_i \\ -w_i/2 & \Delta\zeta_i \end{bmatrix}' + \begin{bmatrix} x_i & y_i \\ x_i & y_i \\ x_i & y_i \\ x_i & y_i \end{bmatrix}', \quad (3)$$

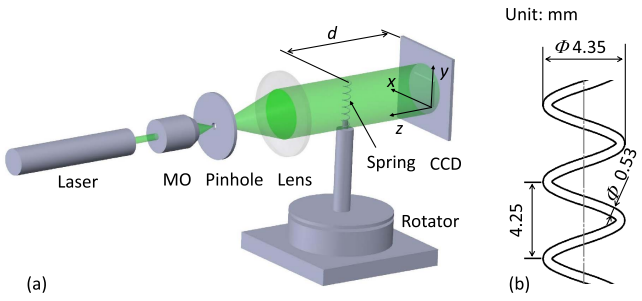

Fig. 1. Schematic of the experimental setup for measuring a stationary stringy object: (a) digital in-line holographic system and (b) the spring being measured.

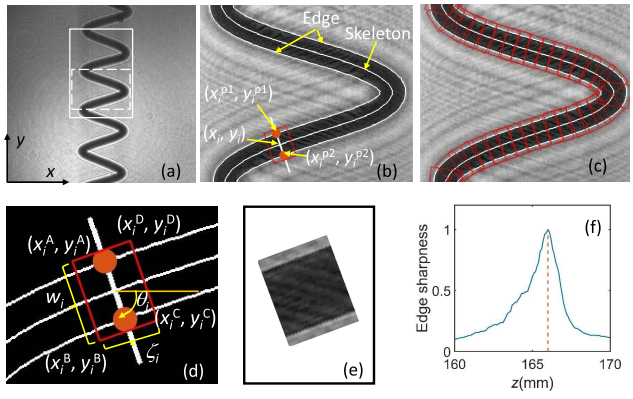

Fig. 2. Automated detection of a stringy object. (a) Typical raw hologram of the spring. Solid box encloses the area of interest that is analyzed, and the dashed box shows one pitch exemplified in (b) and (c). (b) DEI used to identify the edge and the skeleton. (c) Sections enclosed in the red rectangles, with 50% overlapping area. (d) Schematic showing how the section mask is obtained. (e) Extracted section at its focal plane. (f) Normalized edge sharpness of the section in (b) along z direction.

is generated to extract the section images [Fig. 2(e)] from the reconstructed field, so the neighboring sections as shown in Fig. 2(c) have a 50% overlap which gives a smooth transition. The edge of each section is extracted again with an optimal threshold to determine the local diameter ρ_i by applying the hybrid method [11]. The depth position z_i of the same section is identified when the average sharpness on the edge reaches a maximum [Fig. 2(f)]. Furthermore, the surface points of the ith section are obtained and stitched together with other sections to reconstruct the entire object.

The new method is applied to measure the static spring from two reference angles, 0° and 90°, respectively, by adjusting the rotator, as shown in Figs. 3(a) and 3(b). The z–y view at 0° is expected to be the same as the x–y view at 90°. Figure 3(c) compares the measurements of the local diameters to the value measured by a caliper (530 μm). The measured diameter ranges from 502.2 to 558.3 μm, indicating a largest relative error of 5.3%. The section locations are also compared in Fig. 3(d), where r is the distance from the section centers to the spring axis. The r – y profiles at 0° and 90° match well with the largest deviation being 0.23 mm, suggesting an accurate measurement of z locations of the sections. It is noted here that we define the deviation as the distance from a section in 0° to its nearest section in 90° and label this deviation as the red squares in Fig. 3(d). The measured external diameters from the two reference angles are 4.35 and 4.30 mm, respectively, which agree well with the stated value (4.35 mm). The measured pitch is 4.20 and 4.15 mm, respectively, in good accordance with the stated value of 4.25 mm. Thus, the new method is able to characterize the 3D features of a stingy object accurately in an automatic manner.

This method is also used to characterize the dynamic liquid rim in drop breakup. Figure 4 shows the experimental setup. Compressed air is supplied to generate a nearly uniform jet at the exit. A dispensing tip placed above the jet exit releases a water drop. The drop leaves the dispensing tip with near zero velocity and is introduced into the jet by gravity. A mass-flow sensor is used to monitor the total air flow rate in the nozzle such that the air-jet velocity can be adjusted. The Weber number, $We = \rho_a u_0^2 d_0/\sigma$, which describes the ratio of disruptive aerodynamic drag forces to restorative surface tension forces, is about 13, which falls into the bag breakup regime [8]. Here, $\rho_a \approx 1.177$ kg/m^3 is the density of the ambient air, $u_0 \approx$ 16.9 m/s is the initial relative velocity between the air and the drop, $d_0 = 2.78 \pm 0.02$ mm is the initial drop diameter measured using images of 12 drops (as shown in Fig. 4 inset), and $\sigma \approx 0.072$ N/m is the surface tension. The liquid drop is first aerodynamically squeezed into a pancake shape by the air jet and then blown into a bag shape structure attached to a rim. The bag ruptures into smaller droplets, and the rim later breaks up into relatively large droplets [8]. Understanding and modeling the spatial-temporal development of this dynamic process is particularly important in applications in engines, where the presence of smaller drops has a large effect on ignition, while the larger ones control combustion efficiency. A DIH system is set up by recording the holograms of the rim structures using a high-speed camera (Phantom v2512, pixel size of 28 μm × 28 μm) operated at 1,024 × 768 pixels, 31,000 frames per second. The exposure time is 1 μs, short enough to fix the rims and droplets when the same continuous wave laser as that in Fig. 1 is used.

A rim is identified as an object with major axis length larger than 2 mm. Figure 5 shows the rim evolution determined by the present method. The DEIs in Fig. 5(a) indicate that the rim is expanding with time and further fragmenting into ligaments. The morphology varies dramatically, especially in the red and purple rectangles. Within 1.58 ms, the rim breaks up into five ligaments (labeled as Rim 1-5 in Fig. 6) and more small droplets. Figure 5(b) is a 3D visualization of the rim and droplets with all the frames superimposed to show the translation, expansion, and development of the structures. The results show good spatial-temporal continuity, demonstrating the capability of the automated measurement for rim and ligament dynamics. Meanwhile, the total volume ratio of the rim, V_r/V_0, is presented in Fig. 6, where V_r and V_0 are the volumes of the rim and the initial liquid drop, respectively. At the first frame ($t_o + 2.26$ ms), the volume ratio is 0.885. It decreases to 0.31 (red bars) because of the breakup and subsequent atomization. Ligaments (Rim 1-5) forming after the fifth frame in Fig. 5(a) are also characterized. The volume of the rims decreases gradually, except for the sixth frame which may result from heavily overlapped and non-symmetric sections. The volume ratio of the secondary droplets first increases from 0.028 to 0.051, and then decreases to 0.037. The increase is dominated

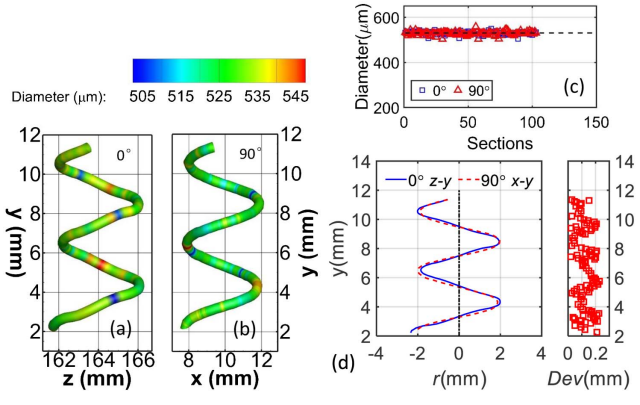

Fig. 3. 3D measurements of a still spring. (a) z–y view of 0°. (b) x–y view of 90° (rotating anticlockwise). (c) Comparison of local diameters. (d) Comparison of spring profiles; the red squares are the deviations at the corresponding y position.

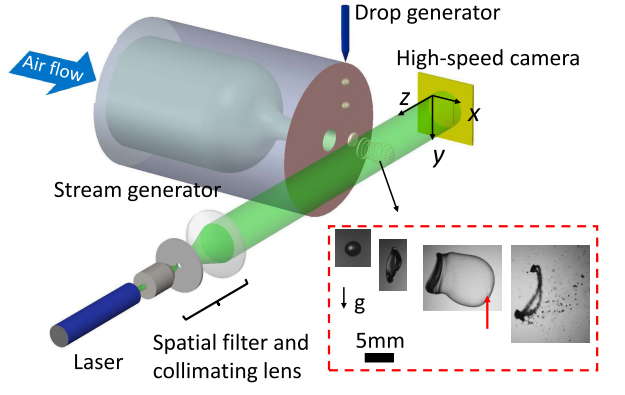

Fig. 4. Experimental setup for the 3D dynamic measurement of the aerodynamic breakup of a falling drop. The inset shows characteristic phases from the intact drop to bag breakup (with an intact rim) recorded by high-speed photography. The red arrow indicates the last moment before the bag raptures.

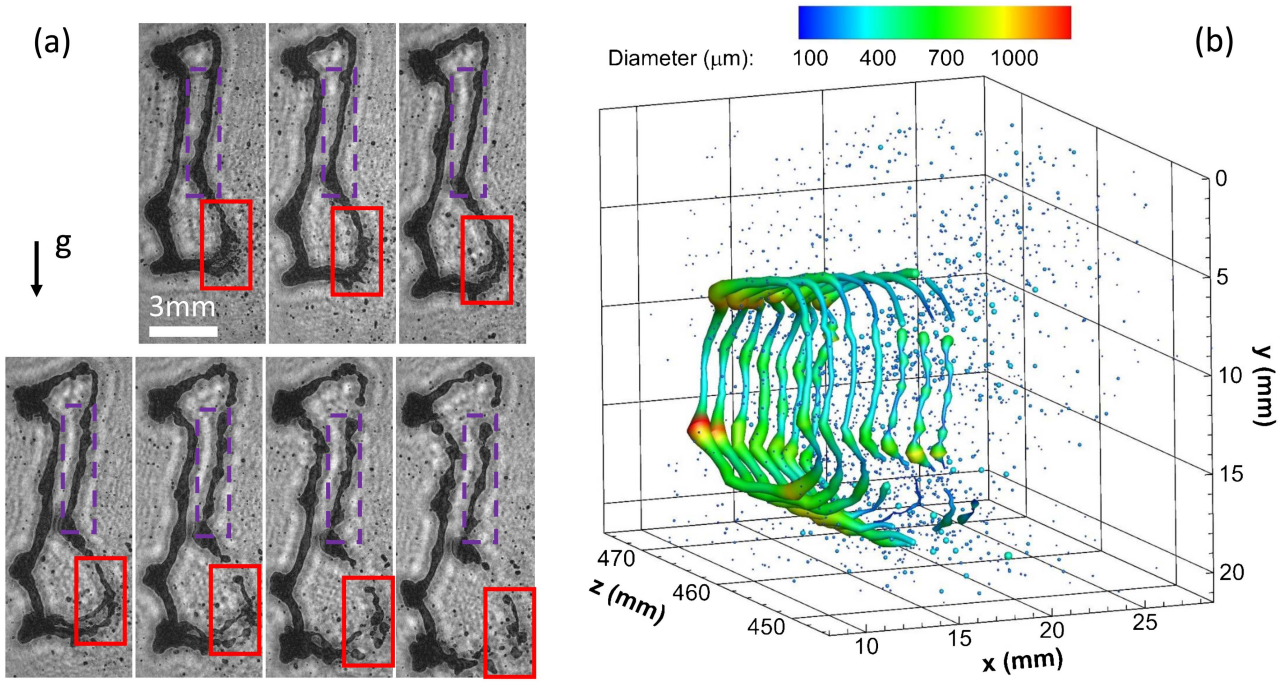

Fig. 5. Spatial-temporal evolution of the rim structure after the bag breaks up. The first frame, taken at 2.26 ms after the start of the bag breakup (red arrow in Fig. 4), is set as the reference (t_o). (a) DEIs at different time instants. The time interval (δt) of any two adjacent frames is 226 μs. The red and purple boxes highlight the region where rim morphologies change dramatically. (b) 3D visualization of the rims of seven selected frames in (a), plotted together with secondary droplets.

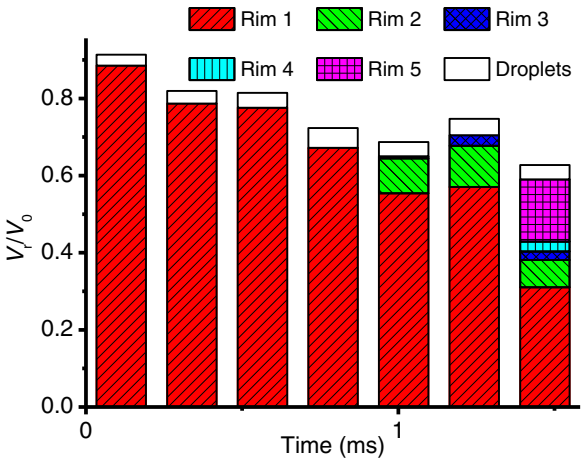

Fig. 6. Temporal evolution of the volume fractions of rims and secondary droplets.

by rim breakup and atomization such as in the red rectangle in Fig. 5(a). On the other hand, as many of the small droplets move out of the field of view, the volume ratio of secondary droplets decreases. There is also a loss caused by evaporation.

In this Letter, it is demonstrated that the dynamic development of a stringy object can be characterized by processing the recorded hologram using the new automated method. This combination provides an excellent tool for studying the spatial-temporal variation of liquid drop breakup, with accurate capture of the local 3D geometries of rim/ligament objects. The results enable further analysis leading to understanding the physics. It is noted that the measurement of the heavily overlapping region might be problematic, which can be partially corrected by choosing an effective illumination angle in the holographic recording stage. In addition, every local section is assumed to be axisymmetric, which may yield less accurate measurement if the section does not have a circular cross section.

Funding. National Natural Science Foundation of China (NSFC) (51576177, 51621005); China Scholarship Council (CSC) (201606320173).

REFERENCES

1. J. Katz and J. Sheng, Annu. Rev. Fluid Mech. **42**, 531 (2010).
2. Y. Wu, X. Wu, J. Yang, Z. Wang, X. Gao, B. Zhou, L. Chen, K. Qiu, G. Gérard, and K. Cen, Appl. Opt. **53**, 556 (2014).
3. Y. Wu, L. Yao, X. Wu, J. Chen, G. Gréhan, and K. Cen, Fuel **206**, 429 (2017).
4. Y. Yang and B.-S. Kang, Opt. Lasers Eng. **49**, 1254 (2011).
5. J. Gao, D. R. Guildenbecher, P. L. Reu, V. Kulkarni, P. E. Sojka, and J. Chen, Opt. Lett. **38**, 1893 (2013).
6. L. Tian, N. Loomis, J. A. Domnguez-Caballero, and G. Barbastathis, Appl. Opt. **49**, 1549 (2010).
7. J. P. Fugal, T. J. Schulz, and R. A. Shaw, Meas. Sci. Technol. **20**, 075501 (2009).
8. D. Guildenbecher, C. López-Rivera, and P. Sojka, Exp. Fluids **46**, 371 (2009).
9. D. Lebrun, A. Benkouider, S. Coëtmellec, and M. Malek, Opt. Express **11**, 224 (2003).
10. M. Kempkes, E. Darakis, T. Khanam, A. Rajendran, V. Kariwala, M. Mazzotti, T. J. Naughton, and A. K. Asundi, Opt. Express **17**, 2938 (2009).
11. D. R. Guildenbecher, J. Gao, P. L. Reu, and J. Chen, Appl. Opt. **52**, 3790 (2013).